AGU PUBLICATIONS

Supporting Information for

"Bayesian seismic source inversion with a 3-D Earth model of the Japanese Islands"

DOI: 10.1002/

Saulė Simutė[1,2], Christian Boehm [1], Lion Krischer [1], Alexey Gokhberg [1,3],

Martin Vallée [2], Andreas Fichtner [1]

[1]Institute of Geophysics, ETH Zurich, Zurich, Switzerland

[2]Université de Paris, Institut de physique du globe de Paris, CNRS, F-75005 Paris, France

[3]Fragata Computer Systems AG, Schwyz, Switzerland

Contents of this file

Introduction

In Text S1 we in more detail describe the seismic velocity model constructed for the Japanese archipelago. This model is used to compute the Green's functions for the seismic source inversion. In Text S2 we describe the procedure of choosing the mean of the prior probability density distribution, which is required for the Bayesian source inversion.

Figures S1 – S5 accompany the description of the velocity model, while figures S6 – S9 and table S1 provide more details of methodology and results of the seismic source inversion.

Text S1. The most important aspects of the full-waveform seismic velocity model building together with the summary of the results are described in the main text, section 2.

Waveform fit improvement. The overall waveform misfit decreased by 24 % after the first seven iterations in the larger initial domain, and by another 21 % during the subsequent seven iterations in the smaller domain. More details on the misfit evolution are shown in Fig. S1.

Tomographic results. The lateral averages $\bar{v}_{sv}$ and $\bar{v}_{sh}$ are shown in Fig. S2. While the depth profiles of our model largely agree with the Preliminary Reference Earth Model (PREM) model (Dziewoński & Anderson, 1981), there are a few deviations. First, the average anisotropy in the upper mantle is less pronounced in our model compared to PREM, which might be surprising given large anisotropy values throughout the model as shown in Fig. S5. The Lehmann discontinuity seen at $\sim$ 220 km depth in PREM, the origin of which is still debated (Karato, 1992; Shito et al., 2006; Revenaugh & Jordan, 1991), is not a universal feature across global models (there is no such a discontinuity in AK135 (Kennett et al., 1995)), and it is not visible in our model either. We use QL6 attenuation model (Durek & Ekström, 1996) to correct the velocities to the reference frequency of 1 Hz. The attenuation model has strong discontinuities at 80 km and 220 km depth, which can probably be attributed to the discontinuities seen at the same depth in Fig. S2.

A collection of depth and cross-sectional slices through the tomographic model in terms of deviation of the isotropic S velocity v_s from the lateral average of $\bar{v}_s$ is shown in Figs. S3 and S4. We compute isotropic S velocity as $v_s = \sqrt{\frac{2}{3}v_{sv}^2 + \frac{1}{3}v_{sh}^2}$ (e.g., Babuška & Cara, 1991; Panning & Romanowicz, 2006).

At the shallow depths (Fig. S3, 30 km) the differentiation between the thinner oceanic crust and thicker continental one is clearly visible. At 30 km depth, mantle velocities are present beneath the oceans and the Sea of Japan, while continental areas are distinguished by lower crustal velocities.

Compared to the tomographic results presented in Simutė, Steptoe, Gokhberg, and Fichtner (2016), more fine-scale features appear at depths between around 30 km and 200 km, where the sensitivity of the fundamental mode surface waves is highest for the periods of 15–80 s (Dahlen & Tromp, 1998) (Figs. S3, S4). The Pacific plate slab at the Japan trench and the Philippine Sea plate slab at the Nankai trough, characterized as positive velocity anomalies, become more pronounced at 100–150 km depth. Negative velocity anomalies associated with the volcanic arc in central Japan, become more localized at shallow depths ($<$ 100 km), while the negative velocity anomaly beneath the Shikoku basin grows stronger in the north, just off the Kii peninsula (Fig. S3, 150 km depth). More fine-scale structure appears beneath Ulleung Island in the Sea of Japan, with strong negative velocity anomalies extending down to $\sim$ 200 km depth (Fig. S4), below which it resembles a narrow tail, well visible at a cross section at latitude 37° (Fig. S4).

While we chose the perturbations of the isotropic S wave velocity in order to give a general view of the velocity anomalies, we note that anisotropy is required to fit the waveforms, and hence we show depth slices of anisotropy computed as $\zeta = \frac{v_{sh}-v_{sv}}{v_s} \times 100$ %. Although, as expected, it is dominated by positive values, meaning v_{sh} is larger than v_{sv}, at depths of 80 km and deeper, areas of negative anisotropy arise (Fig. S5).

Text S2.

In this section we describe the procedure for choosing the mean of the prior probability density for the Bayesian source inversion.

We run a preliminary inversion for all the study events at periods of 15–80 s. For this initial sampling we use automatically selected measurement windows over the main energy part of the trace, use the Global Centroid-Moment-Tensor (GCMT) solution (The Global CMT Project, 2021) as a prior mean, and run the inversion for 5×10^4 samples. If the synthetic data for the maximum-likelihood solution provide a significantly better waveform fit than the GCMT solution, we use it as a prior mean for the main inversion, both for constrained and unconstrained scenarios.

For two out of three events, for which the 15–80 s period band proved to be the acceptable inversion period band (20040407, 20050816), the prior mean model is updated. We perform this preliminary step at all period-band inversions for these two events. Hence, at each inversion period band, these events have different priors (Fig. S6).

For events which could not be inverted at the shortest-period band, we always use the GCMT solution as a prior mean. Omitting the preliminary inversion step was done due to the time constraints. In short, for all the events with an acceptable period band other than 15–80 s, the GCMT solution is used as a prior mean.

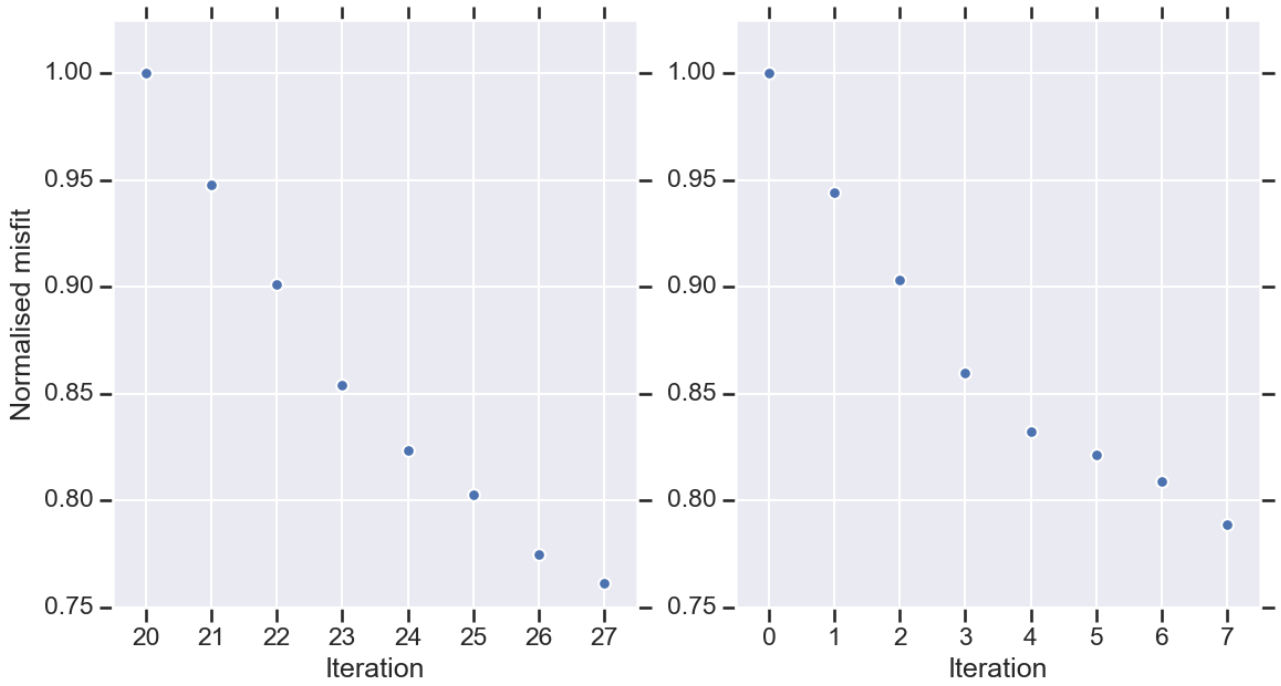

Figure S1. Per-iteration misfit reduction for measurement windows in the period band of 15–80 s, computed for time-frequency misfit as used in the inversion. **Left:** waveform fit improved by 24 % in the first seven iterations run with the original model setup. **Right:** waveform fit improved further by 21 % after seven iterations run with the new model setup as shown in Fig. 1.

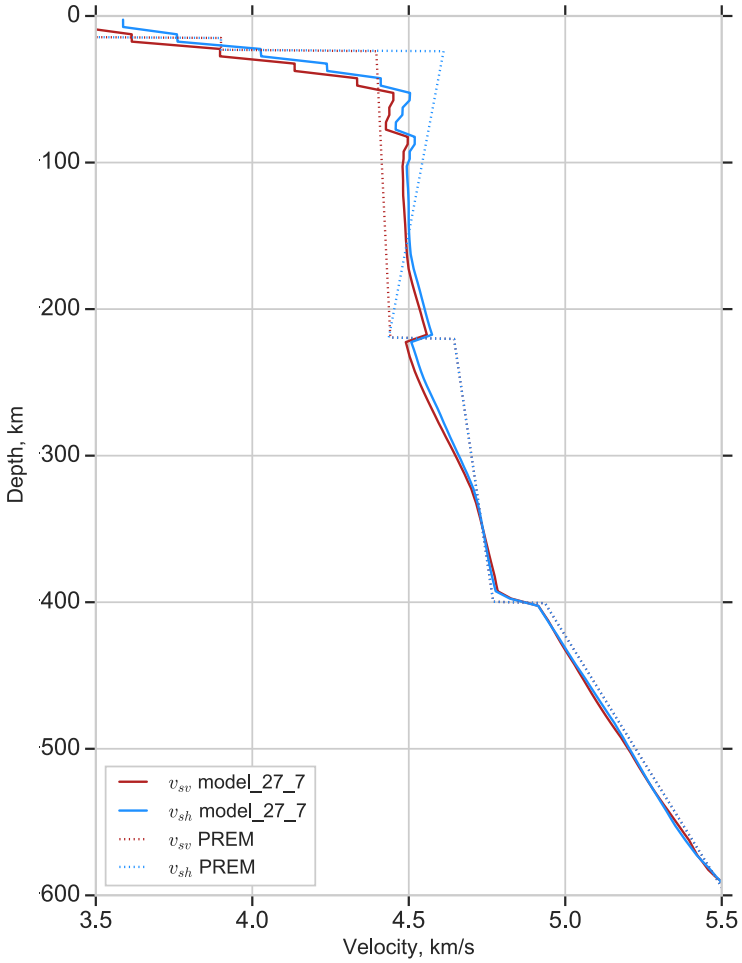

Figure S2. Lateral averages of the updated model of v_{sv} and v_{sh} at a frequency of 1 Hz. The equivalent velocities for the radially symmetric PREM are shown for comparison (Dziewoński & Anderson, 1981).

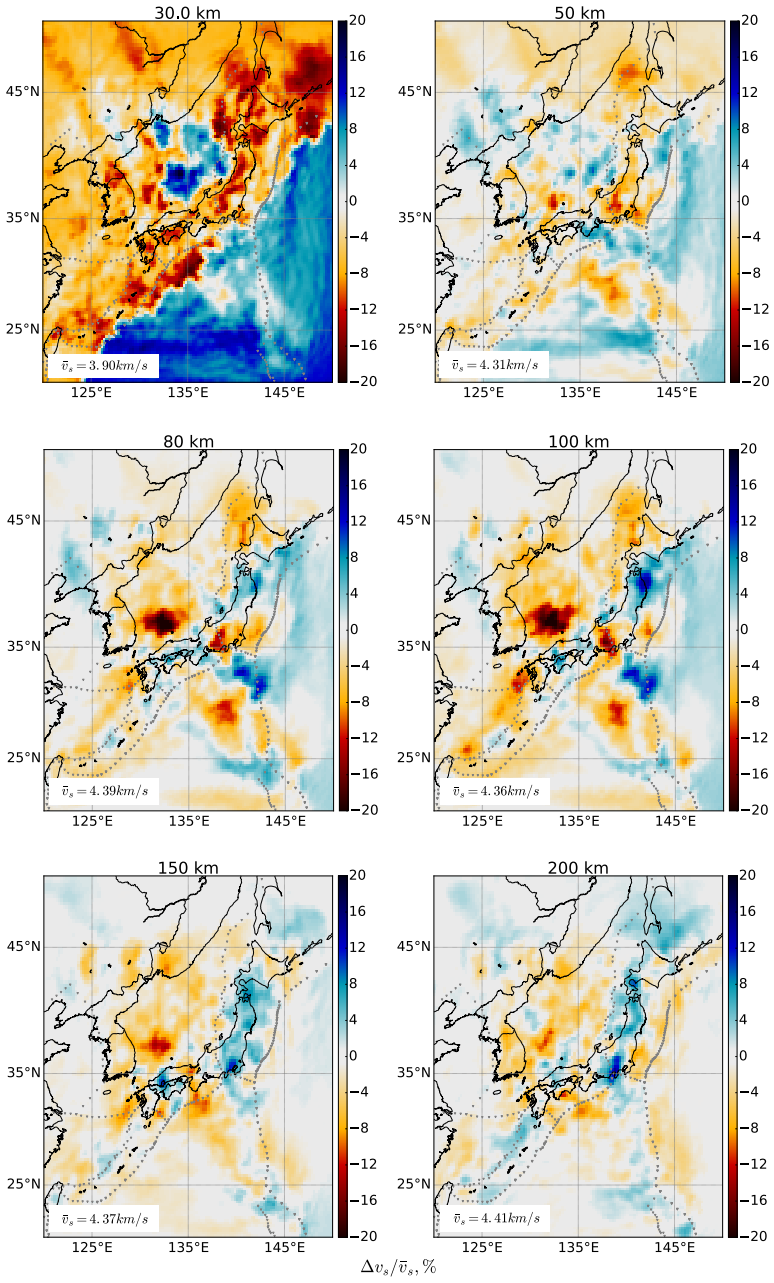

Figure S3. Depth slices of isotropic v_s perturbations across the model domain. Perturbation is computed as $\frac{v_s - \bar{v}_s}{\bar{v}_s} \times 100$ %, where $\bar{v}_s$ is the lateral average of v_s for each depth. At 30 km depth we can see the mantle velocities in the Pacific ocean as well as the Sea of Japan. The negative velocity anomaly in the Sea of Japan is strongest in amplitude and extent between 80 and 100 km depths. Positive velocity anomalies are associated with the subducting Pacific and Philippine Sea slabs. Dashed gray lines represent plate boundaries.

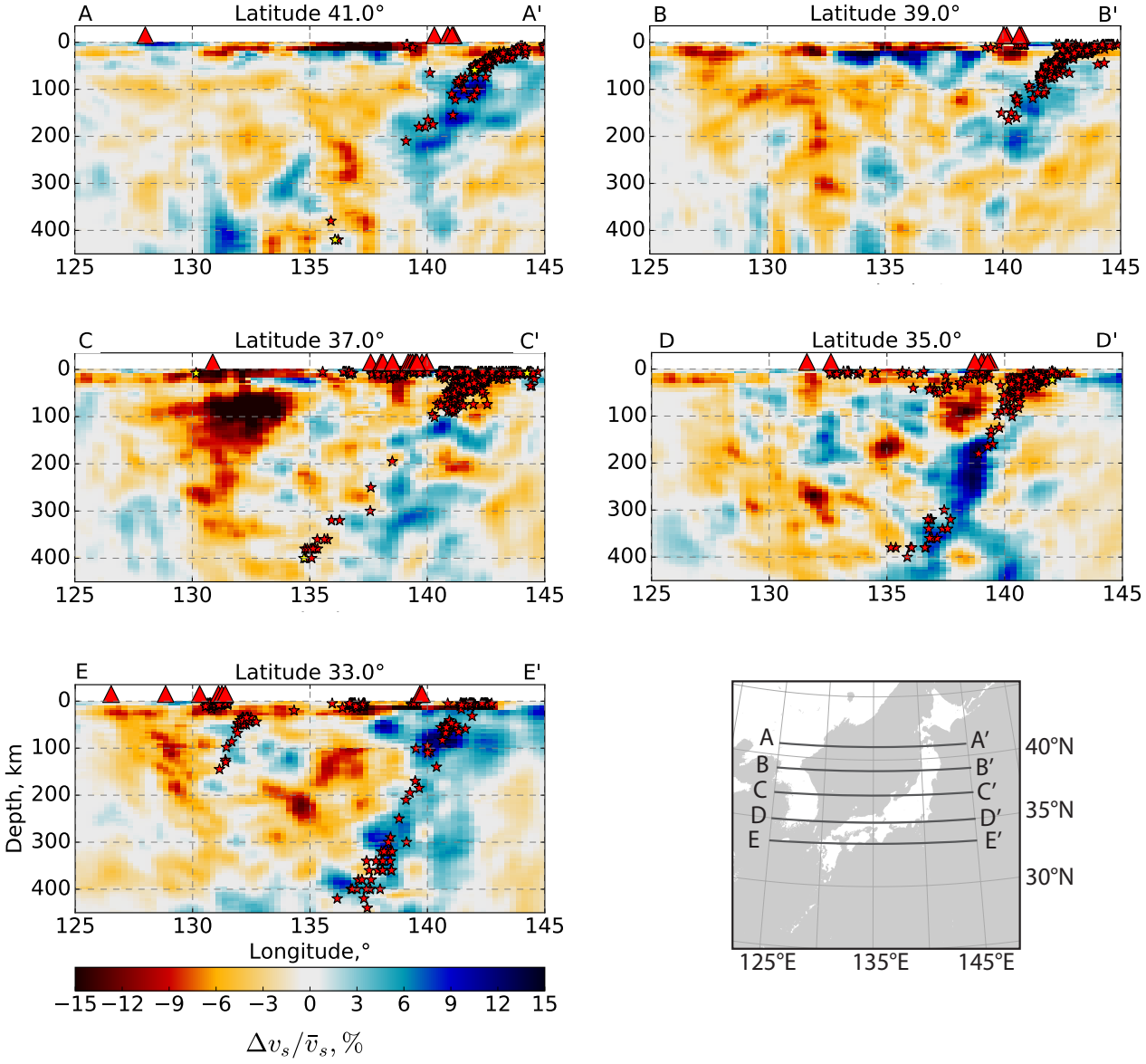

Figure S4. Cross-sections through the isotropic v_s perturbations in the model domain. Red and yellow stars represent earthquakes since 1997 and earthquakes used in this study, respectively, within 1° of the slice. Red triangles represent Holocene volcanoes (Siebert et al., 2010).

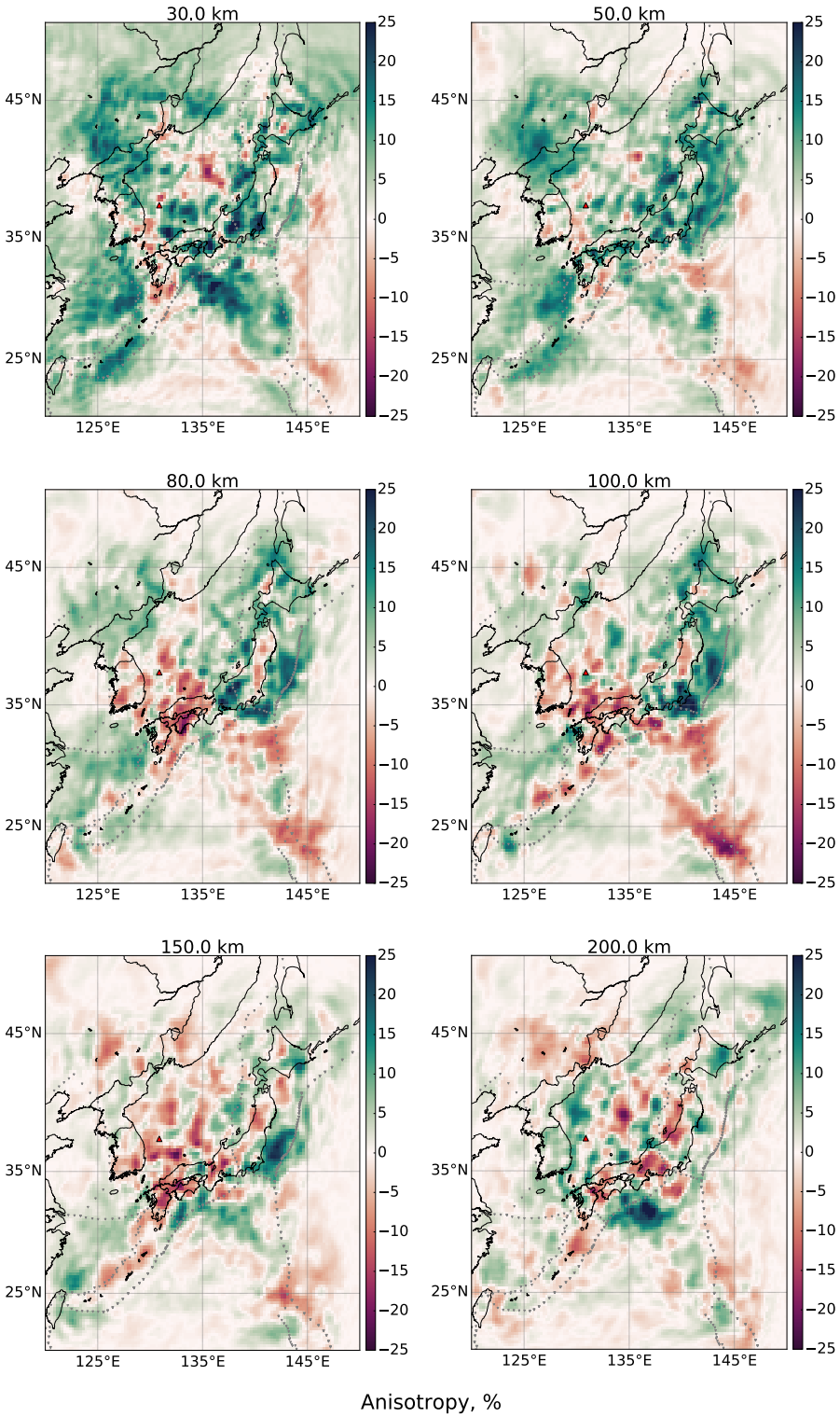

Figure S5. Radial anisotropy $\zeta = \frac{v_{sh}-v_{sv}}{v_s} \times 100\%$ for selected depth slices across the model domain.

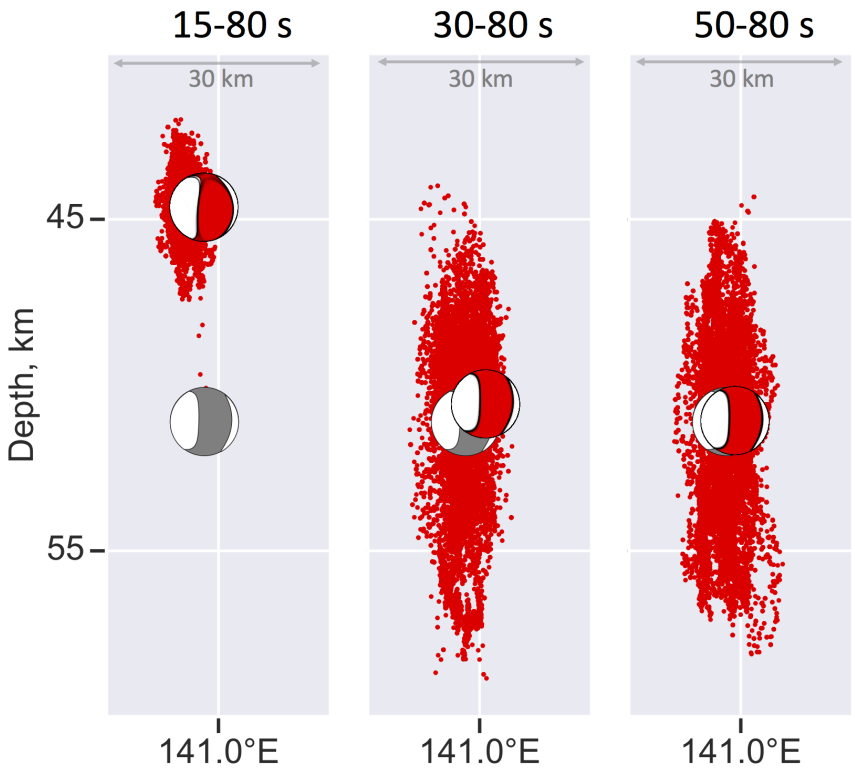

Figure S6. Ensembles of the location for event 20050816 after the preliminary inversions, performed in order to update the location used as a prior mean in the main inversions. The results are for three period bands, i.e., 15–80 s, 30–80 s, and 50–80 s. Red dots represent the accepted models from the unconstrained inversions. The maximum-likelihood models from each inversion are shown as red focal mechanisms, and they are used as prior means in the main inversions. Gray beachballs represent the GCMT solution, which was used as a prior mean in each of these preliminary runs.

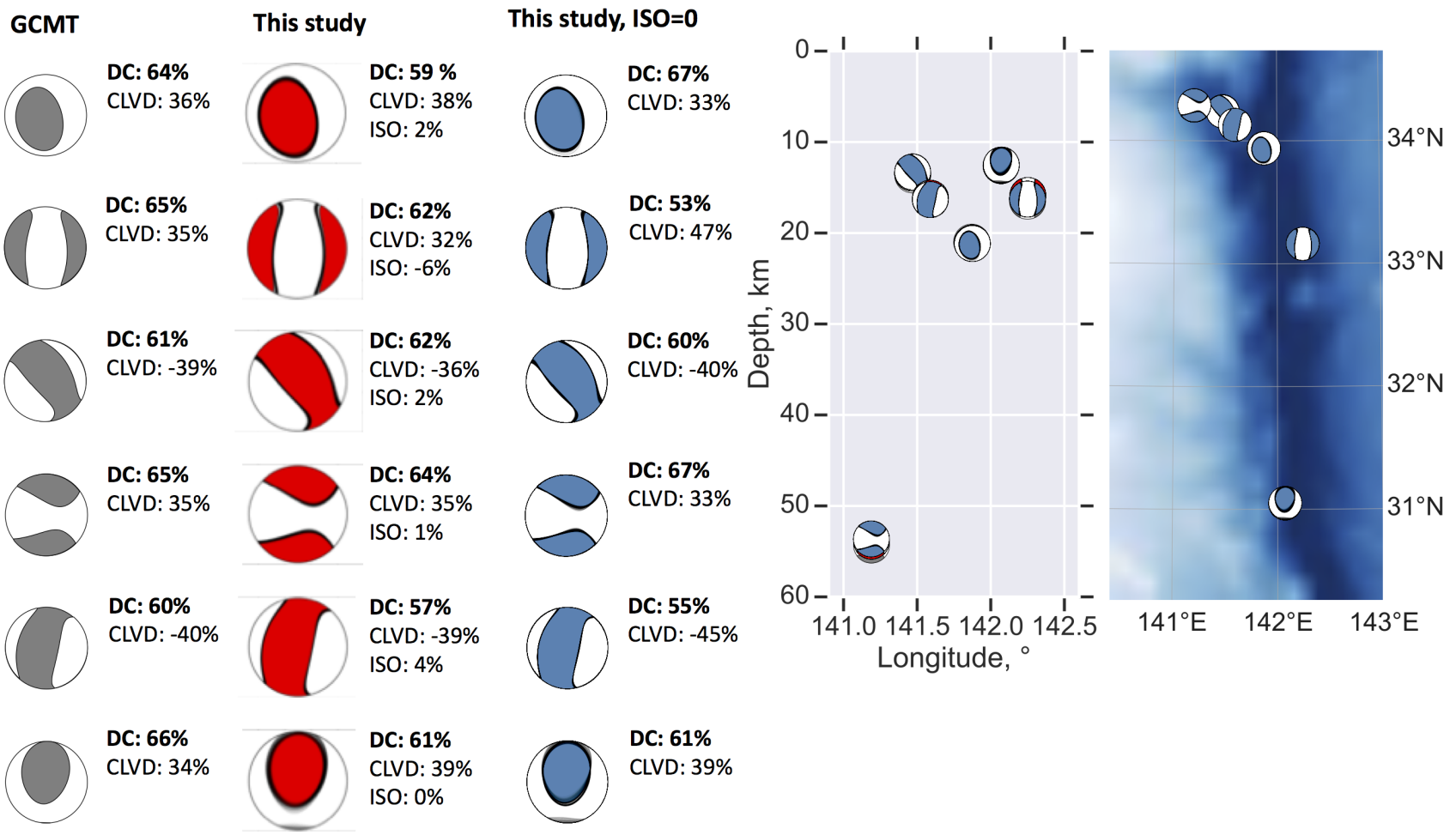

Figure S7. Moment tensor ensembles inferred with 50–80 s period data (events in the third, fourth and fifth rows are also presented in the main text). Gray beachballs correspond to the GCMT solution, red beachballs correspond to an unconstrained inversion, and blue ones correspond to the inversion, where we assume no volumetric component. Gray lines represent every 100th model of the ensemble, with the maximum-likelihood models colored. On the right, we show the maximum-likelihood locations, following the same color code.

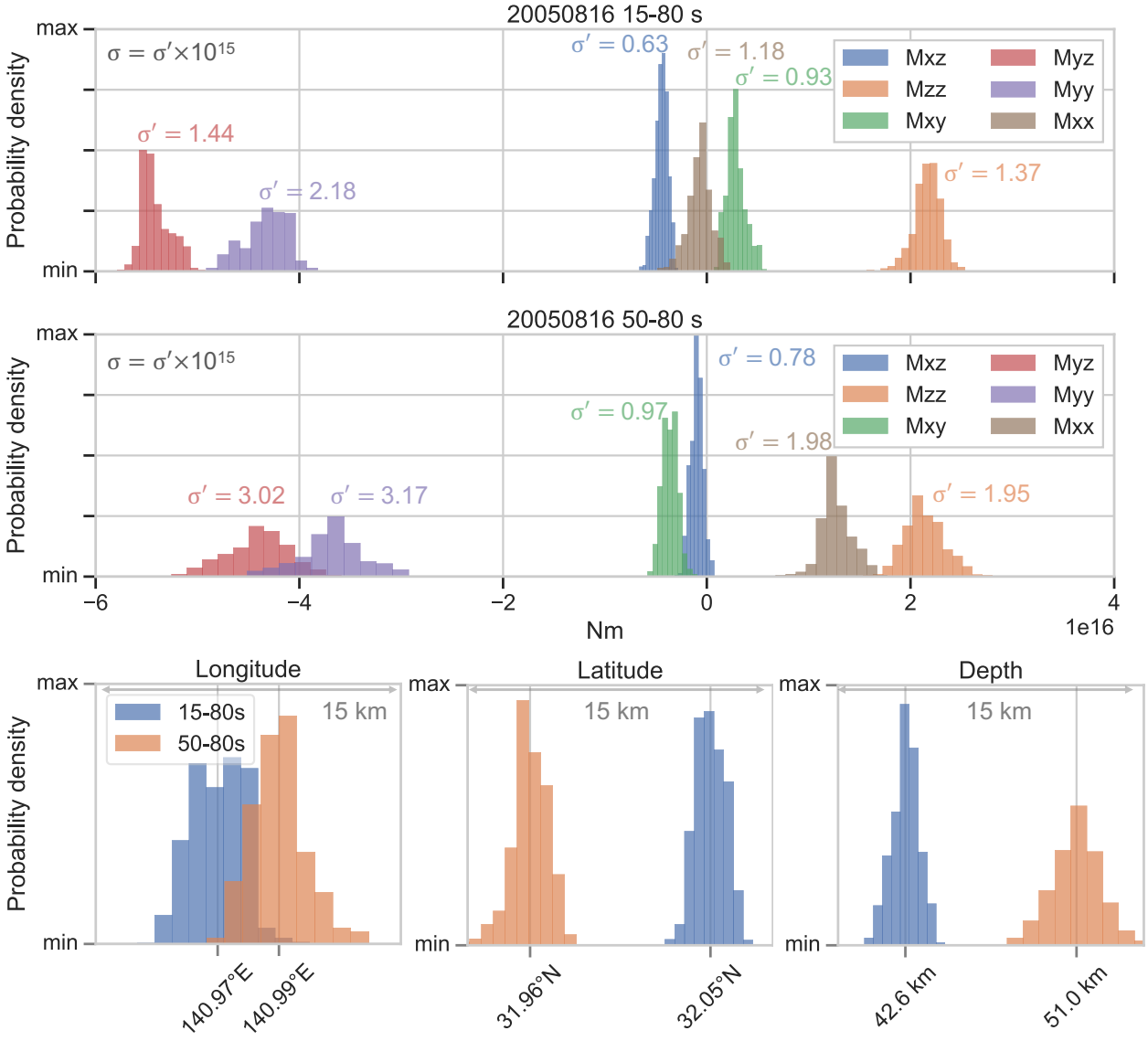

Figure S8. Comparison of marginal probability densities inferred with 15–80 s and 50–80 s data for event 20050816. Marginal probability densities for moment tensor elements with standard deviation values are shown in the top two graphs. Marginal probability densities for location parameters are shown below. Generally, shorter-period inversion better constrains the inversion parameters, especially the diagonal elements (M_{xx}, M_{yy}, M_{zz}) of the moment tensor and depth.

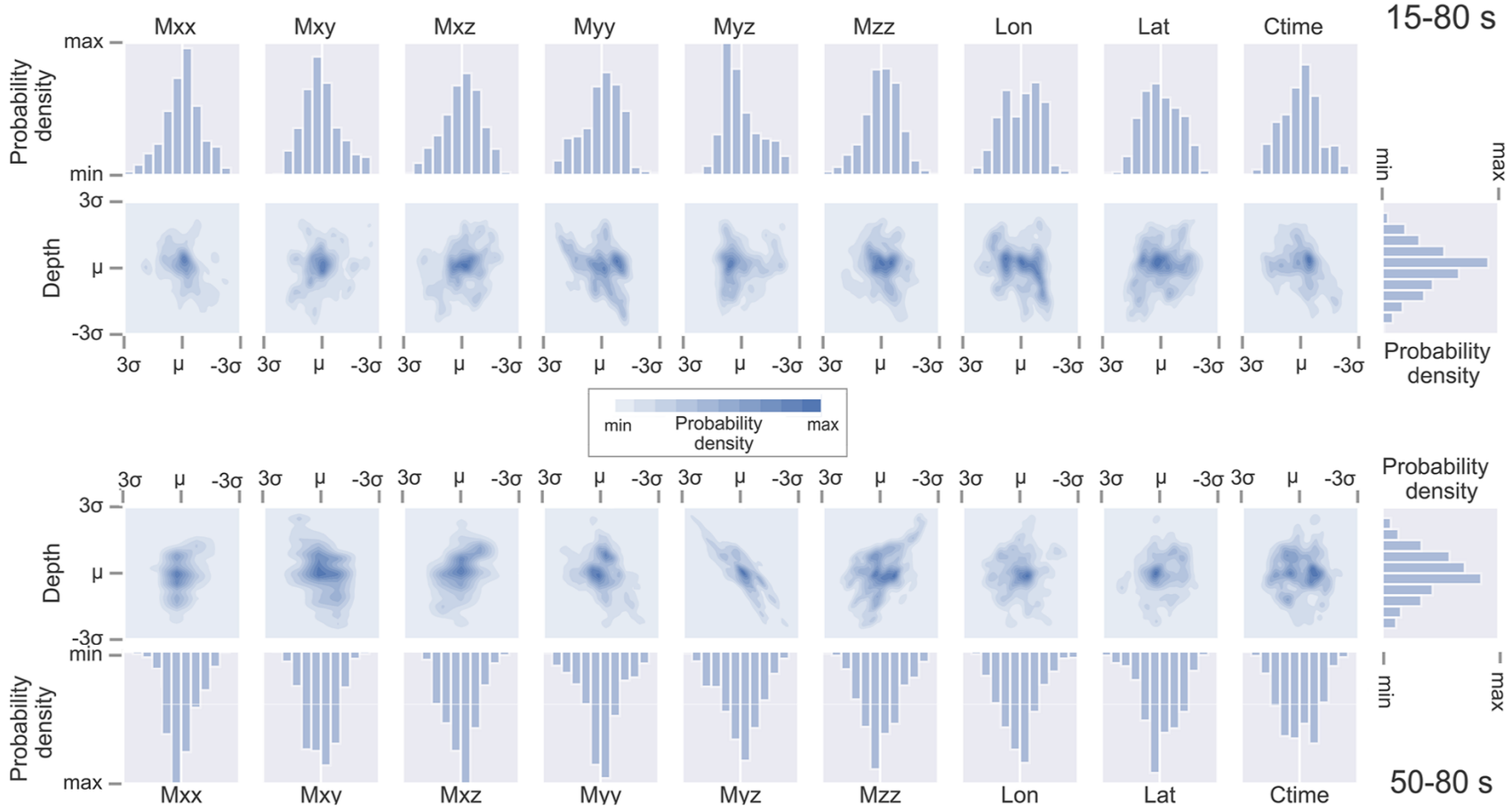

Figure S9. Comparison of selected trade-offs and marginal probability density functions for 15–80 s (top) and 50–80 s (bottom) period data inversion of event 20050816. The limits for each parameter depend on the corresponding standard deviations, and are set from $\mu - 3\sigma$ to $\mu + 3\sigma$, where μ is the mean and σ is the standard deviation of the distributions. At long periods, depth has considerable trade-offs with M_{yz} and M_{zz} components, but the parameters are much better constrained when short period data are used.

January 14, 2022, 5:36pm

Event ID	Date	Origin time	Lon	Lat	Depth, km	Seismic moment, 1e16 Nm	CLVD, %
15 – 80 s							
20170506	2017-05-06	14:23:17.4	140.78	33.21	56.9	3.488	-52
20040407	2004-04-07	13:47:02.7	140.50	34.27	45.1	4.836	-62
20050816	2005-08-16	19:15:34.2	140.98	31.96	51.1	5.606	-47
20 – 80 s							
20121126	2012-11-26	20:08:00.8	141.9	33.43	16.1	2.049	48
30 – 80 s							
20151105	2015-11-05	08:23:03.5	140.99	32.20	42.8	5.388	-20
20071120	2007-11-20	11:46:31.4	141.01	32.68	42.2	3.787	7
20140527	2014-05-27	16:12:10.5	140.78	32.59	63.6	2.837	-35
50 – 80 s							
20101129	2010-11-29	15:02:11.0	141.87	33.94	21.0	2.690	36
20050204	2005-02-04	18:34:13.7	142.25	33.16	16.5	3.831	35
20150314	2015-03-14	15:36:08.8	141.47	34.24	13.6	4.811	-39
20050924	2005-09-24	14:48:48.3	141.19	34.29	54.3	7.49	35
20111116	2011-11-16	00:43:58.1	141.59	34.13	16.3	9.73	-40
20150508	2015-05-08	12:11:29.6	142.07	31.05	12.6	2.370	34

Table S1. Information on the study events, as given in the GCMT catalog (The Global CMT Project, 2021). Earthquakes are grouped according to their shortest acceptable inversion period band.

References

Babuška, V., & Cara, M. (1991). *Seismic anisotropy in the Earth.* Kluwer Academic Publishers, Dordrecht, Boston, London.

Dahlen, F. A., & Tromp, J. (1998). *Theoretical Global Seismology.* Princeton University Press. NJ.

Durek, J. J., & Ekström, G. (1996). A radial model of anelasticity consistent with long-period surface wave attenuation. *Bull. Seis. Soc. Am.*, *86*, 144-158.

Dziewoński, A. M., & Anderson, D. L. (1981). Preliminary reference Earth model. *Phys. Earth Planet. Inter.*, *25*, 297–356.

Karato, S.-I. (1992). On the Lehmann discontinuity. *Geophysical Research Letters*, *19*(22), 2255-2258. doi: https://doi.org/10.1029/92GL02603

Kennett, B. L. N., Engdahl, E. R., & Buland, R. (1995). Constraints on seismic velocities in the Earth from traveltimes. *Geophys. J. Int.*, *122*, 108-124.

Panning, M., & Romanowicz, B. (2006). A three-dimensional radially anisotropic model of shear velocity in the whole mantle. *Geophys. J. Int.*, *167*, 361-379.

Revenaugh, J., & Jordan, T. H. (1991). Mantle layering from ScS reverberations: 3. The upper mantle. *J. Geophys. Res. Solid Earth*, *96*(B12), 19781-19810. doi: https://doi.org/10.1029/91JB01487

Shito, A., Karato, S., Nishihara, Y., & Matsukage, K. (2006). Towards mapping the tree-dimensional distribution of water in the upper mantle from velocity and attenuation tomography. In S. D. Jacobsen & S. van der Lee (Eds.), *Earth's deep water cycle, geofigure 14. summary of seismological observations and theoretical and experimental results with respect to rs/p. b03308 shito et al.: Attenuation and velocity in izu-bonin 12 of 13 b03308 earth's*

deep water cycle, geophys. monogr. ser (Vol. 168, p. 225-236). AGU, Washington, D. C.

Siebert, L., Simkin, T., & Kimberley, P. (2010). *Volcanoes of the world, 3rd edition.* University of California Press.

Simutė, S., Steptoe, H., Gokhberg, A., & Fichtner, A. (2016). Full-waveform inversion of the Japanese islands region. *J. Geophys. Res.*, *121*, 3722-3741.

The Global CMT Project. (2021). *Moment Tensor Product Query.* Retrieved 8th November 2021, from `https://ds.iris.edu/spud/momenttensor`